Structure and stability of the low-index surfaces of Fe_3Si: *Ab initio* density functional investigations

J. Hafner* and D. Spišák†

Fakultät für Physik and Center for Computational Materials Science, Universität Wien, Sensengasse 8, A-1090 Wien, Austria

(Received 18 December 2006; published 9 May 2007)

We present a detailed *ab initio* density functional study of the composition, structure, and stability of the low-index surfaces of $D0_3$-type Fe_3Si. For the ferromagnetic low-temperature phase, we predict a general tendency toward a Si enrichment of the surface, in agreement with experiment. We show that the observed surface phase transitions are strongly coupled to the magnetic phase transition in the bulk. Quite strong structural relaxation effects are predicted for the more open (100) and (111) surfaces.

DOI: 10.1103/PhysRevB.75.195411 PACS number(s): 68.35.−p, 71.15.Nc, 75.50.Bb, 81.30.Bx

I. INTRODUCTION

The current interest in iron-rich silicides is based on a wide range of potential applications, ranging from the use as structural materials over magnetic applications to the use as diffusion barriers and contacts in microelectronics.[1] The most iron-rich compound, Fe_3Si, has a high magnetic susceptibility; hence, this phase is of great interest as a soft magnetic material. Fe_3Si/FeSi multilayers have been studied because of their giant magnetoresistance behavior.[2,3] Very recently, Fe_3Si films epitaxially grown on semiconducting substrates (Si, GaAs) have raised strong interest due to their potential use in magnetoelectronic devices, e.g., for spin injection in semiconductors.[4–7] Chemical-vapor deposition was used to produce stable Fe_3Si coatings in SiFe steels characterized by high hardness, good corrosion resistance, and high electrical resistivity.[8] The promising properties of iron silicide films have triggered a considerable interest in their surface properties.

At room temperature, three homogeneous iron silicide phases of different stoichiometries exist in the bulk phase diagram.[9] Among those, Fe_3Si crystallizing in the $D0_3$ structure (BiF_3 type, Pearson symbol cF16)[10–13] is the only well-ordered iron-rich phase. In the $D0_3$ unit cell (see Fig. 1), Fe atoms occupy the α and γ sublattices and Si atoms the β sublattice such that the distance between Si atoms is maximized. Stoichiometric Fe_3Si exhibits $D0_3$ order up to its incongruent melting point at 1220 °C. The phase field of $D0_3$-type $Fe_{1-x}Si_x$ alloys extends over the composition range $0.15 < x < 0.25$. Fe_3Si orders ferromagnetically, with a Curie temperature decreasing with decreasing Fe content, reaching a value of $T_c \sim 450$ K at the stoichiometric composition.

In phases with a silicon concentration lower than ideal, β sites are occupied randomly by Fe and Si. At Si concentration below 10%, the $D0_3$ phase is replaced in a very narrow composition range by a $B2$ (CsCl-type) phase in which β and γ sites are occupied randomly by Fe and Si. At still lower Si content, all sites are randomly occupied by Fe and Si, forming a substitutionally disordered $A2$ (body-centered-cubic) phase. At elevated temperatures, also more Si-rich compounds undergo a $D0_3$ to $B2$ transition, and the transition temperature increases from about 800 °C at 15 at. % Si to 1200 °C for the nearly stoichiometric alloy. On the Si-enriched side, an abrupt transition from the ordered $D0_3$ phase to an inhomogeneous phase region is observed. The compositional asymmetry observed in the phase stabilities is also reflected in the atomic mobilities: In Fe_3Si, the diffusion of the majority component (Fe) is orders of magnitude faster than that of the minority component (Si); Fe diffusion is also strongly composition dependent (diffusion is fastest in the nearly stoichiometric alloy).[14–18] The anomalous diffusion properties of Fe_3Si have also attracted considerable theoretical interest; recent *ab initio* density functional calculations in combination with a statistical-mechanical analysis have demonstrated that the dominant species of defects characterized by the lowest formation energies are Fe antisite atoms in the β sublattice and Si antisite atoms on the γ sublattice, followed by Fe vacancies on the α and γ sites, while the formation energies for Si vacancies and Si antisite atoms on the α sublattice are significantly higher.[19]

At higher Si content, two ordered phases exist at room temperature: ϵ-Fe adopting the $B20$ (Pearson symbol cP8, space group $P2_13$) structure and β-$FeSi_2$ crystallizing in an orthorhombic lattice (Pearson symbol oC48, space group *Cmca*).[9,12,13] In thin films, however, different structures than in the bulk are observed over the entire composition range. Epitaxially stabilized Fe-Si films with a 1:1 stoichiometry crystallize in a defective $B2$ structure,[20,21] while for films with a 1:2 stoichiometry a structure related to α-$FeSi_2$ (CaF_2 type, Pearson symbol tP3, space group $P4/mmm$) has been proposed.[22,23] Ultrathin Fe_3Si films do not develop well-ordered structures, while ordered $D0_3$-type films have been reported for larger thickness.[24]

Experimental characterizations of the surface structures have been performed on thin-film samples and on low-index surfaces prepared on single-crystal specimens.[23,25–29] For CsCl-type FeSi films grown on Si(111), quantitative low-

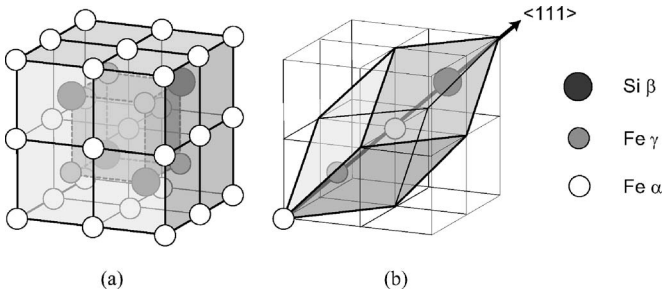

FIG. 1. The $D0_3$ structure: (a) 16-atom cubic cell and (b) 4-atom primitive cell.

energy-electron-diffraction (LEED) experiments, supplemented by density functional theory (DFT) calculations, have shown that the surface is Si terminated and shows an unusual multilayer relaxation of +6%, −16%, and +14% from the top layer into the bulk, which has been interpreted in terms of a strong covalent bonding between the subsurface iron atoms and the adjacent Si layers.[28] For single-crystal $Fe_3Si(100)$ surfaces, Busse *et al.* reported [based on LEED, Auger electron spectroscopy (AES), photoelectron spectroscopy, and ion scattering spectroscopy] Si surface segregation, leading to the formation of an ordered CsCl double layer on top of the $D0_3$-type bulk. Starke *et al.*[26] found two temperature-induced surface phase transitions on $Fe_3Si(100)$. Both the low- and high-temperature phases have (1×1) periodicity with the full two-dimensional symmetry of the $D0_3$ crystal structure, while the intermediate phase has $c(1\times1)$ periodicity. For the low-temperature phase, the LEED analysis suggests a model consisting of a bulklike layer stacking with an additional Si layer on top of a mixed Fe-Si layer. Subsequent work by the same group[27] using LEED and AES slightly modified this picture and extended the analysis to the (110) and (111) surfaces. Reversible transitions between an ordered low-temperature (LT) phase stable below 400 °C and a partially disordered high-temperature (HT) phase formed at about 600 °C were reported for all three surfaces. The transition between the LT and HT phases is reversible, but rather slow; it is induced by a reversible surface segregation of Si on all three surfaces. It is a striking coincidence that the formation of the HT phase takes place in the same temperature range as the ferromagnetic to paramagnetic phase transition in bulk Fe_3Si. Si termination is preferred in any case, either by the choice of a topmost Si layer (where this possibility exists) or by the formation of Si antisite defects. Si surface enrichment was also reported for Fe-rich Fe-Si alloys.[29]

The present work is devoted to *ab initio* density functional studies of the structure and stability of all three low-index surfaces of Fe_3Si. The stability of a large number of different structural models is calculated as a function of the chemical potential above the surface, including the investigation of the influence of magnetic ordering on the surface phase stability.

II. COMPUTATIONAL DETAILS

Our calculations are based on density functional theory in the local spin-density approximation using the Vienna *ab initio* simulation package[30] (VASP). VASP performs an iterative solution of the Kohn-Sham equations in a plane-wave basis. The ion-electron interaction is treated within the projector augmented wave (PAW) formalism.[31] The advantage of the PAW method over the commonly used pseudopotential construction is that the effective one-electron potential is based on accurate all-electron charge and spin densities.

The energy cutoff for the plane-wave representation of the wave functions is set to 300 eV, ensuring a good convergence of total energies. We used the local exchange-correlation functional parametrized according to Perdew and Zunger[32] with nonlocal corrections in the form of the generalized gradient approximation proposed by Perdew *et al.*[33]

To simulate the low-index Fe_3Si surfaces, we used periodically repeated supercells containing 9, 8, and 15 atomic layers for the (100), (110), and (111) surfaces, respectively. A vacuum region of more than 10 Å served for suppressing interactions between adjacent slabs. The surface unit cell contained four atoms for all three surface orientations. For the (100) surface, this corresponds to a doubling of the (1×1) surface unit cell of the $D0_3$ structure. For the (110) surface, our choice corresponds to the (1×1) surface unit cell of the parent lattice, and for the (111) surface to a (2×2) periodicity. For the (100) and (110) surfaces, the positions of the atoms in the outermost four layers were relaxed such as to minimize the total energy, while for the (111) surface, which undergoes more severe relaxations, as many as seven layers were included in the geometry optimization. The structural relaxation was achieved using a damped Newton algorithm until the residual forces on every movable ion dropped below 10 meV/Å^2. Brillouin-zone integrations were based on Monkhorst-Pack grids.[34] A $6\times6\times1$ grid with 12 k points in the irreducible wedge of the two-dimensional Brillouin zone was used for the (100) surface, a $8\times6\times1$ grid with 12 k points for the (110) surface, and a $5\times5\times1$ grid with 13 k points for the (111) surface. To improve convergence, we employed a Methfessel-Paxton smearing[35] of 0.15 eV. Atom-resolved magnetic moments were obtained by integration of the spin densities within atomic spheres with a radius of 1.30 Å for Fe and 1.31 Å for Si. Since the magnetic moments on the Si ions are very small (of the order of $0.1\mu_B$, aligned opposite to the magnetic moments of the surrounding Fe atoms), they are not specified in the following.

The results for bulk Fe_3Si, body-centered-cubic (bcc) Fe, and Si in the diamond structure are compiled in Table I. The lattice constants agree with experiment within 1% for the pure elements and for the intermetallic compound. The calculated bulk moduli of the elements fall into the range spanned by the available experimental data; for Fe_3Si, we note good agreement with the results of Drickamer *et al.*[42] Very good agreement is also achieved for the magnetic moments. For a more detailed discussion of the density functional results for the properties of bulk Fe_3Si, we refer to the work of Dennler and Hafner[19] based on the same computational method. This work also contains a detailed calculation of the phonon spectrum, the defect-formation and -migration energies.

III. *AB INITIO* THERMODYNAMICS OF SURFACES

We have systematically investigated the stability and properties of the low-Miller-index surfaces of Fe_3Si, allowing for variations in the chemical composition of the near-surface layers. However, a direct comparison of the total energies of slabs representing surfaces with different stoichiometries is meaningless. In such cases, one must include the relevant particle reservoirs, characterized by the chemical potentials of both atomic species. The chemical potential measures the energy required to add a particle to the system. Since the chemical potentials depend on temperature and

TABLE I. Comparison of calculated and experimental structural parameters and magnetic moments of Si, Fe, and Fe_3Si in the diamond, body-centered-cubic, and $D0_3$ crystal structures, respectively. a, cubic lattice parameter; B, bulk modulus; B', pressure derivative of the bulk modulus at zero pressure; m, the magnetic moment in the ferromagnetic (FM) state.

		Si	Fe		Fe_3Si	
Pearson symbol		$cF8$	$cI2$		$cF16$	
Space group		227	229		225	
		NM	NM	FM	NM	FM
a (Å)	Calc.	5.473	2.699	2.837	5.528	5.602
	Expt.	5.431[a]		2.860[b]		5.65[c]
B (GPa)	Calc.	88	270	169	263	227
	Expt.	81[d]		168[e]		250[f]
		99[e]		173[g]		
B'	Calc.	3.47	5.83	5.25	8.29	8.60
m_{Fe} (μ_B)	Calc.			2.25		2.56, 1.34
	Expt.			2.22[e]		2.2–2.4,1.35[h]
m_{Si} (μ_B)	Calc.					−0.08
	Expt.					−0.07[h]

[a]Reference 36.
[b]Reference 37.
[c]Reference 12.
[d]Reference 38.
[e]Reference 39.
[f]Reference 42
[g]Reference 41.
[h]Reference 40.

pressure, this allows us to extend the results of DFT calculations obtained at zero temperature to realistic experimental conditions. The combination of first-principles DFT calculations with statistical mechanics in the grand-canonical ensemble has been described in detail in Refs. 43–45.

The thermodynamic stability of a given surface is determined by its surface free energy per unit area,

$$\gamma(T,p,\{p_i\}) = \left[G(T,p,\{n_i\}) - \sum_i n_i \mu_i(T,p_i) \right] \Big/ A, \quad (1)$$

where T denotes temperature, p is the pressure, G is the Gibbs free energy of the slab with a surface area of A, and n_i and μ_i are the number of atoms and the chemical potential of the species of i (i=Fe or Si) at the partial pressure p_i. For not too high temperatures, the vibrational and configurational contributions to the Gibbs free energy typically do not exceed values of 10 meV/Å^2 (Ref. 45), and in addition these contributions are of comparable magnitude for comparable surfaces; therefore, the Gibbs free energy will be approximated by the total energy E obtained from DFT. The requirement of the thermal equilibrium between the Fe and Si particle sources and the bulk Fe_3Si crystal is expressed by the condition

$$3\mu_{Fe} + \mu_{Si} = g_{Fe_3Si}, \quad (2)$$

where g_{Fe_3Si} is the Gibbs free energy per formula unit of bulk Fe_3Si. Inserting Eq. (2) into Eq. (1) leads to the surface energy as a function of the chemical potential of Fe only,

$$\gamma = [E - n_{Si} g_{Fe_3Si} - (n_{Fe} - 3n_{Si})\mu_{Fe}]/A. \quad (3)$$

The chemical potential μ_{Fe} can be varied only in a limited range. If it is too high, the Fe_3Si crystal is unstable with respect to the formation of compact Fe islands on the surface; therefore,

$$\mu_{Fe} \leqslant g_{Fe}, \quad (4)$$

where g_{Fe} is the Gibbs free energy of bcc Fe as the most stable Fe phase. On the other hand, if the chemical potential of Fe is too low, the crystal is unstable against segregation of silicon and the formation of Si crystallites on the surface. Therefore, the second constraint for μ_{Fe} reads

$$\mu_{Fe} \geqslant (g_{Fe_3Si} - g_{Si})/3. \quad (5)$$

The region of the permissible values of μ_{Fe} is indicated by a gray area in the following pictures. As all surface structures are modeled in a supercell geometry, the straightforward approach for the application of Eq. (1) is to use a symmetric slab with two equivalent surfaces. In our calculations, the bottom of the slab is always frozen with an unrelaxed bulklike termination of the $D0_3$ structure, and only the composition of the upper part surface is modified and its structure relaxed. In order to correct for the asymmetric slabs, the surface energy of a symmetric, unrelaxed and bulklike terminated slab has been calculated separately and subtracted from the total surface energies.

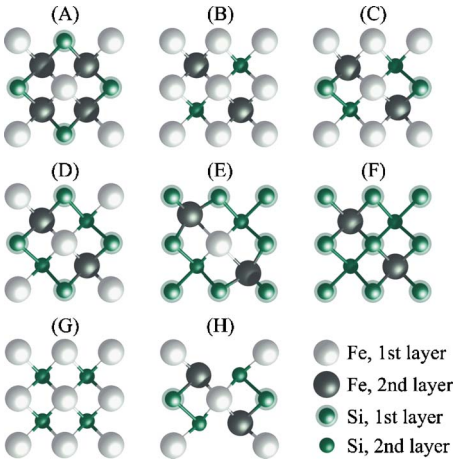

FIG. 2. (Color online) Possible surface geometries of the $Fe_3Si(100)$ face. (A) A bulk-terminated surface with a mixed Fe-Si occupation (Fe in γ sites, Si in β sites) of the top layer. (B) A bulk-terminated surface with only Fe atoms in the α sites in the surface layer. (C) As model (B) with one Fe atom replaced by Si. (D) As model (B) with two Fe atoms replaced by Si atoms. (E) As model (B) with three Fe atoms replaced by Si atoms. (F) A Si surface layer on top of a bulklike stacking sequence of mixed Fe-Si and pure Fe layers, starting with a mixed Fe:Si layer. (G) An Fe/Si/Fe trilayer on top of a $D0_3$-like layer stacking. (H) A mixed Fe-Si surface as in model (D) with a Si vacancy.

IV. STABILITY, GEOMETRY, AND MAGNETIC STRUCTURE OF $Fe_3Si(100)$ SURFACE

A. Surface phase stability

Perpendicular to the [100] direction, the Fe_3Si crystal may be cleaved either at a plane with a mixed Fe:Si occupation in a ratio 1:1 or at a plane occupied by Fe atoms only. These two bulklike terminations are displayed in Fig. 2 as configurations (A) and (B). In addition, we have examined six further possible surface structures compatible with the periodicity of the $D0_3$ cube. Because the LEED study[27] concluded that a significant redistribution of atoms takes place merely in the two uppermost layers, we have constructed models varying the chemical occupation of the sites in the surface and subsurface. In our surface unit cell with four atoms in a plane, the concentration may be varied in steps of 25%, allowing us to simulate roughly the existence of disordered phases. Configurations (C)–(F) are derived from the bulklike Fe-terminated surface B by successively replacing Fe in the surface layer by Si (creating Si antisite defects on the α sublattice) while leaving the mixed occupation of the subsurface layer unchanged. The second subsurface layer is occupied by Fe only, defining a $D0_3$-like stacking sequence. In model (D), both top layers have an ordered 1:1 occupation by Fe and Si. In model (F), where Fe has been completely replaced by Si, a pure-Si layer is placed on top of bulk-terminated crystal. This corresponds to the model advocated in the first publication by Starke *et al.*[26] Model (G) represents a termination by a CsCl-type Fe/Si/Fe trilayer. This model differs from model (B) by creating a Si_β antisite defect. Finally, model (H) is derived from model (C) by creating vacancy in the surface layer, as suggested by Busse *et al.*[25] Hence, the surface layer of model (H) contains a Si_α antisite defect and an α vacancy.

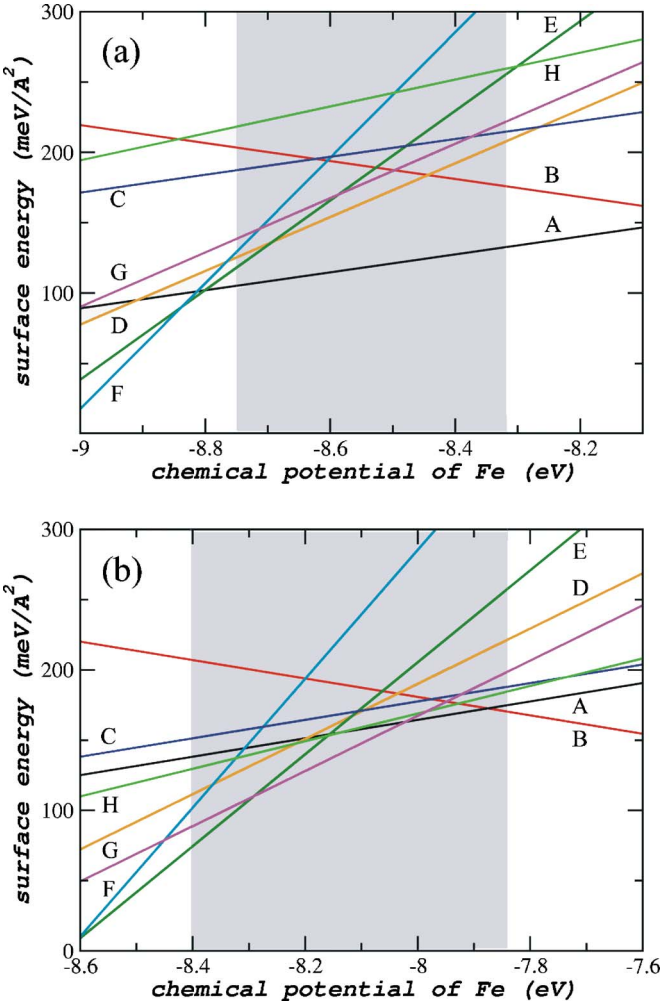

FIG. 3. (Color online) Surface free energy as a function of the chemical potential of Fe for different possible configurations of an $Fe_3Si(100)$ surface. (a) The results shown in the top panel are calculated for a ferromagnetically ordered slab; (b) those in the bottom panel are based on a nonmagnetic calculation. The letters A–H denote different surface configurations displayed in Fig. 2.

The surface phase diagrams calculated for ferromagnetic and nonmagnetic Fe_3Si are shown in Fig. 3. The lines with a negative slope identify the models with an excess of iron atoms compared to the stoichiometric concentration; hence, these configurations become more stable under Fe-rich conditions (high pressures and low temperatures). Phase stability is strongly influenced by magnetic ordering.

In the ferromagnetic phase of Fe_3Si stable below the Curie temperature, the only stable surface geometry is configuration (A) with a bulklike stacking terminated by a mixed Fe:Si layer. At the upper limit of the admissible values of Fe chemical potential, the least favorable configurations are those with an enhanced Si content—models (F) and (E)—or containing surface vacancies (H). This reflects the large energies required for creating Si antisite defects or vacancies on the α sublattice in bulk Fe_3Si (see Ref. 19). At the lower limit of the chemical potential, the energies of these Si-

TABLE II. Vertical interlayer relaxations Δd, buckling amplitudes b, and magnetic moment on Fe atoms calculated for the surface and subsurface layers. The values are given for all stable terminations of the ferromagnetic low-index Fe_3Si surfaces. The interlayer distances in the bulk are $d_{100}=1.401$ Å, $d_{110}=1.981$ Å, and $d_{111}=0.809$ Å.

Surface model	Δd_{12} (%)	b_1 (Å)	Δd_{23} (%)	b_2 (Å)	m_1 (μ_B)	m_2 (μ_B)
(100) A	−5.4	0.11	3.9	0.00	2.84	1.50, 1.52
(110) B	0.3	0.05	0.5	0.04	2.05, 2.66	1.48, 2.50
(110) D	−0.4	0.10	0.1	0.12	1.68	1.04, 2.52
(111) A	−14.6	0.00	−33.9	0.00		0.95

enriched surfaces are strongly decreased but still remain higher in energy than the bulk-terminated mixed surface (A).

Nonmagnetic calculations lead to an entirely different picture, with low structural energy differences between different surface models. In the Fe-poor range with $-8.4\ \text{eV} \leqslant \mu_{\text{Fe}} \leqslant -8.3$ eV, a strongly Si-enriched surface [75% Si in the surface layer, 50% Si in the subsurface layer according to model (E)] is predicted to be stable. Further, over a large range of μ_{Fe} from −8.3 to about −8.03 eV model (G) with an Fe/Si/Fe trilayer on top of a bulklike stacking sequence is stable, followed by models (A) and (B) in the Fe-rich limit.

In the ferromagnetic LT phase, the surface cell of model (A) retains the full $D0_3$ symmetry, denoted as (1×1), in agreement with the LEED analysis. The surface shows a mixed Fe:Si occupancy, also in agreement with experiment. In addition, a further Si enrichment by the formation of Si antisite defects on two top layers of the γ and α sublattices has been proposed, but this has not been explored by our models. In the nonmagnetic HT phase, the surface periodicity of model (G) stable over the widest range of the chemical potential corresponds to a smaller $c(1\times1)$ surface cell, i.e., to a CsCl surface structure. Again, this is in agreement with the systematic extinctions of diffraction spots noticed in the LEED measurements.[27] The experimental observation of a $c(1\times1)$ surface periodicity is also compatible with a disordered bcc structure. The AES measurements suggest a Si enrichment of the surface in the high-temperature nonmagnetic phase compared to the low-temperature ferromagnetic phase. This led to the conjecture of a Si/Fe/Si termination. We have not examined this particular stacking (because here the composition in the third layer also varies), but our calculations show that model (F) with a Si/50%Si+50%Fe concentration profile simulating a strongly Si-enriched surface comes out as one of the least stable configurations. In configurations (E) and (G) stabilized at low partial pressures of Fe, the concentration ratios Fe:Si in the two top layers are 3:5 [model (E)] and 1:1 [model (G)], also compatible with a surface enrichment in Si compared to the 3:1 stoichiometry of the bulk. For temperatures above 700 °C, a disordered bcc surface structure has been suggested.[27] The formation of a disordered phase is in accordance with the small energy differences between the possible surface configurations calculated for the nonmagnetic phase.

B. Geometric and magnetic properties

The geometric properties of the various surface configurations also differ. Table II lists the interlayer relaxations, buckling amplitudes, and magnetic moments of the first two layers of the (100) surface in the ferromagnetic LT phase, and in Table III the geometric parameters of the nonmagnetic HT phases are summarized. The interlayer relaxations are calculated for the center of mass of each layer, and the buckling amplitude measures the largest difference in the vertical coordinates within each layer. In the LT phase, only configuration (A) is stable. As observed for most metallic surfaces, the mixed top layer relaxes inward and undergoes a modest buckling of 0.11 Å (the Fe atoms relaxing outward), while the second interlayer distance is expanded. The magnetic moment of the surface Fe atoms is enhanced by $0.3\mu_B$ compared to the bulk value, and likewise the magnetic moments of the subsurface layer are larger by $0.2\mu_B$ compared to those the compact Fe layer in the Fe_3Si crystal. The magnetic moments of the deeper layers are the same as in the bulk.

Quite different relaxation patterns are predicted for the four surface structures that can exist in the HT phase. For the metal-terminated surfaces (G) and (B), a strong inward relaxation of the top layer by about 14% followed by an expansion of the second interlayer spacing is calculated. The two phases differ mainly by a more pronounced buckling of the mixed subsurface layer in model (B). In contrast, surfaces (E) and (A) with a mixed occupation of the top layer expand. In configuration (E), we note a strong expansion also of the second interlayer spacing and a very strong buckling of both the surface and the subsurface layers with one of the Si surface atoms protruding by about 0.8 Å and a contracted Fe atom. The weak binding of a Si atom reflects an incipient tendency to desorb Si from the surface. Unfortunately, no

TABLE III. The interlayer vertical relaxations Δd and buckling amplitudes b for the surface and subsurface layers. The values are given for all stable terminations of the nonmagnetic low-index Fe_3Si surfaces. The interlayer distances in the bulk are $d_{100}=1.382$ Å, $d_{110}=1.954$ Å, and $d_{111}=0.798$ Å.

Surface model	Δd_{12} (%)	b_1 (Å)	Δd_{23} (%)	b_2 (Å)
(100) A	2.3	0.09	−1.9	0.00
(100) B	−14.6	0.00	7.2	0.17
(100) E	5.5	1.06	14.2	0.45
(100) G	−13.4	0.00	4.6	0.03
(110) D	0.8	0.28	0.3	0.15
(111) A	−1.8	0.00	−87.1	0.00

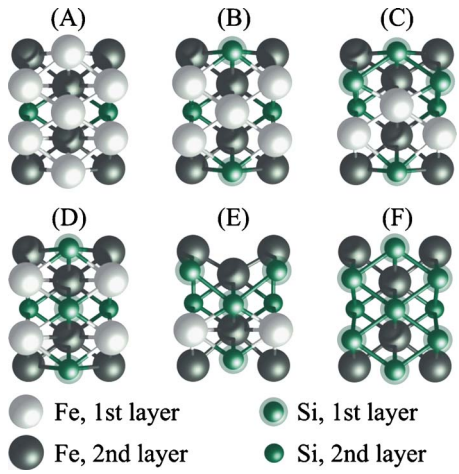

FIG. 4. (Color online) Surface geometries of the $Fe_3Si(110)$ surface. The content of Si atoms in the surface cell varies from 0 to 4 passing from model (A) to model (F). The bulklike termination is represented by model (B). See text.

atomically resolved data of the surface geometry are available from experiment. Starke *et al.*[27] announced a forthcoming publication of data derived from tensor LEED, but this seems not to have been published so far.

V. STABILITY, GEOMETRY, AND MAGNETIC STRUCTURE OF $Fe_3Si(110)$ SURFACE

A. Surface phase stability

In the $D0_3$ structure, all (110) planes are equivalent, and cleavage of the Fe_3Si crystal perpendicular to the [110] direction leads to a surface with the same composition as the bulk. This surface is shown in Fig. 4 as model (B). This surface contains on the α sublattice two Fe atoms in a low-spin state, one Fe atom in a high-spin state on the γ sublattice, and one Si atom on a β site. To construct other models for this surface, we have used a $D0_3$ (1×1) surface cell with four atoms per layer and the composition of the surface layer was allowed to vary. The models shown in Fig. 4 include the whole range of concentrations from a compact Fe layer (Fe antisite defect on the β sublattice), model (A), through increasing content of Si, models (B)–(E), up to a pure-Si layer, model (F). Models (C) and (D) have the same surface composition of 50% Si and 50% Fe, just in a different arrangement, with a Si_α (C) or a Si_γ (D) antisite atom, respectively. Model (E) contains a Si_α antisite defect and a γ vacancy, while model (F) has two Si_α and one Si_γ antisite defects.

The surface phase diagram derived from the variation of the surface free energies with chemical potential displayed in Fig. 5 shows that irrespective of the magnetic state the most stable surface is represented by model (D) with an equal concentration of Si and Fe in the surface layer, corresponding to a surface enriched in Si. Model (C), with the same surface composition but a reduced symmetry and positions of the Si and Fe atoms allowing the formation of direct Fe-Fe and Si-Si bonds, has a surface energy higher by almost 50 meV/Å^2. This fact indicates that clustering of Si atoms in

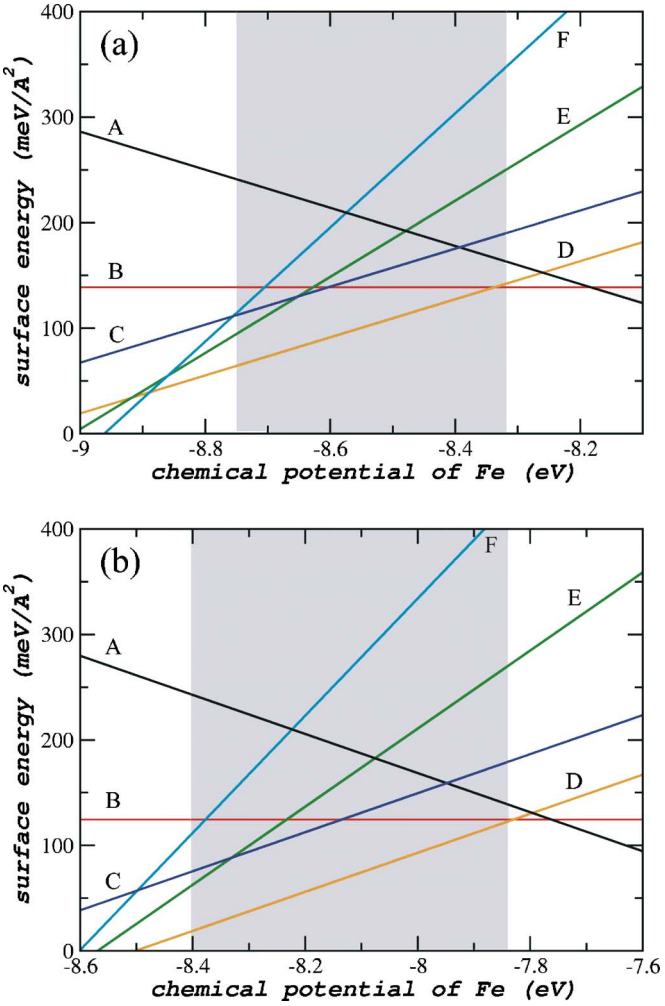

FIG. 5. (Color online) The surface phase diagram for $Fe_3Si(110)$ surface in contact with reservoirs of Fe and Si atoms. (a) The top panel assumes a magnetic calculation, while (b) the bottom panel assumes a nonmagnetic calculation. The letters A–F denote different surface configurations displayed in Fig. 4.

the surface is energetically unfavorable. The energetic preference for model (D) over model (C) also shows that the defect formation energies calculated for the bulk are also a reasonable guideline for the surface: In the bulk, the formation of an antisite defect on an α site [as in model (C)] requires an energy of 1.9 eV, whereas for a Si antisite defect on γ as in model (D), the energetic penalty is only 0.4 eV (after Dennler and Hafner[19]). For model (D), the surface has a smaller unit cell than the bulklike surface (B) [Starke *et al.*[27] use the notation $(\frac{1}{2}\times1)$ for the LEED pattern compared to the (1×1) periodicity of model (B)]. Note that model (C) with the same stoichiometry retains the (1×1) periodicity.

For the LT phase, the LEED analysis[27] suggests a silicon-terminated surface with a (1×1) periodicity and an almost complete replacement of Fe on γ sites in the surface layer, with only a few antisite defects in the subsurface layer. The AES signal ratio suggests an Fe:Si ratio of 3.6 (i.e., no Si enrichment)—one has to remember that AES also probes deeper layers as compared to LEED. This confirms that Si enrichment is restricted to a narrow surface region. The con-

centration profile derived from the tensor-LEED analysis (cf. Fig. 5 in Starke *et al.*[27]) agrees with our preference for model (D). However, it is not quite clear how, with a complete replacement of Fe on γ sites by Si, the surface periodicity is not reduced.

In the HT phase, certain LEED spots disappear and the new phase produced after annealing displays a $(\frac{1}{2}\times 1)$ LEED pattern compatible with our model (D). The AES analysis leads to a concentration ratio of Fe:Si=2.6 for the near-surface layers. On the basis of the tensor-LEED analysis, it is reported that in the surface layer the phase transition leads to only modest changes in the site occupation (not only the β sites but also the γ sites are occupied almost exclusively by Si atoms), leading to a surface stoichiometry of Fe:Si=1:1. In addition, the formation of a certain concentration of β and γ antisite defects in the subsurface layers and the formation of Fe vacancies on α sites in the surface layer have been reported. These possibilities have not been tested by our models, because this would require larger surface cells.

B. Geometry and magnetic properties

The calculated interlayer relaxations are small, below 1%, for both the ferromagnetic and the nonmagnetic phase (see Tables II and III). This is as expected for this close-packed phase; the (110) surface also has a lower surface energy compared to the (100) and (111) surfaces. The relatively strong buckling predicted for a nonmagnetic phase is caused by upward displacements of the Si atoms having Si atoms as second-nearest neighbors in the second layer Si atoms. In the stable configuration (D), the magnetic moments of Fe atoms in low-spin (γ) sites of the surface layer are enhanced by about $0.3\mu_B$ compared to the bulk, while the high-spin α sites are now occupied by Si. For the bulk-terminated surface (B), we note a strong enhancement of the Fe moments on the low-spin sites by $0.7\mu_B$, whereas only a modest enhancement of $0.1\mu_B$ is noted for the high-spin sites.

VI. STABILITY, GEOMETRY, AND MAGNETIC STRUCTURE OF $Fe_3Si(111)$ SURFACE

A. Surface phase stability

The [111] direction corresponds to the long body diagonal of the primitive rhombohedral cell of the $D0_3$ structure containing four atoms: two Fe on α sites, one Fe on γ sites, and one Si on the β sublattice. Each (111) plane is occupied by atoms of the same type; hence, the unit surface cell contains just one atom per layer. Adjacent Si planes are separated by three Fe layers. This surface can have four bulklike terminations differing just by the near-surface layer stacking. Models of these surfaces are shown in Fig. 6. Model (A) is Si terminated with the following three layers occupied by Fe; models (B)–(D) are Fe terminated, with stacking sequences FeSiFe… (B), FeFeSi.. (C), and FeFeFeSi.. (D). Besides, to explore eventual surface segregation phenomena we considered models (E) and (F) derived from model (D) with a (2×2) surface cell containing 50% Si and 50% Fe in the surface layer [two Si_α antisite defects, model (E)] or 25% Fe and 75% [three antisite defects, model (F)], and the following two subsurface layers being occupied by Fe only.

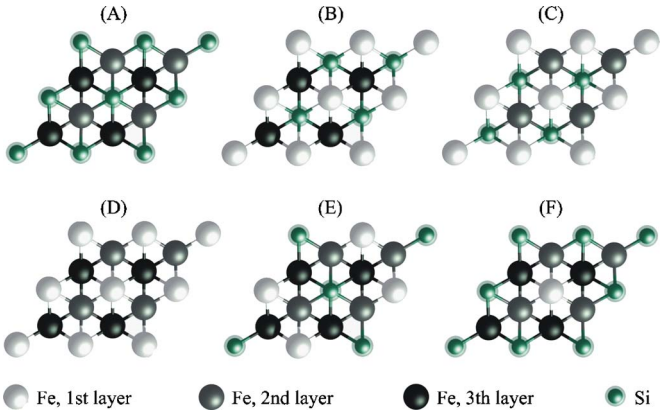

FIG. 6. (Color online) Surface geometries probed for the $Fe_3Si(111)$ face. Models (A)–(D) represent bulk-terminated surfaces exposing one of the four surfaces in the SiFeFeFe… stacking sequence. Model (E) has a mixed Fe-Si surface layer followed by the bulk stacking sequence Fe/Fe/Si.... Model (F) is similar to model (E) but with 25% Fe and 75% Si atoms in the surface layer.

The surface phase diagram derived from the variation of the surface free energies with the chemical potential of Fe plotted in Fig. 7 shows that the only stable termination is that with a Si layer on top, both in the ferromagnetic and the nonmagnetic phases [model (A)]. On the other hand, the surface terminated by an iron trilayer is clearly disfavored. For this surface, the size and shape of the surface unit cell are the same for the $D0_3$, CsCl, and disordered bcc phases. Hence, no distinction is possible on the basis of the LEED pattern alone. From the temperature dependence of the Auger ratio,[27] a Si enrichment has been deduced for the HT phase. The tensor-LEED analysis shows that the Si enrichment occurs in the second subsurface layer only, where in the HT phase Fe in γ site is almost completely substituted by Si, while the first and third subsurface layers containing Fe in α sites contain only a modest number of antisite defects. That the formation of Si_γ defects is much more likely than that of Si_α antistructure atoms agrees with the defect formation energies for bulk Fe_3Si, but a surface modification beyond the second layer has not been tested in the present study.

B. Geometric and magnetic properties

The amount of surface relaxation depends very strongly on the magnetic state of the surface. In addition, on the rather open (111) surface relaxation also affects deeper layers—only after optimization of the coordinates of as many as seven layers convergence of the forces acting on the atoms to the required low level could be achieved. In the ferromagnetic LT phase, the top Si layer relaxes inward by −14.6%, the following Fe layer by −33.9%, the third layer occupied by Fe relaxes outward by a comparable amount (+32.8%), and even the fourth (Fe), fifth (Si), and sixth (Fe) layers still relax by −9%, −7%, and +8%, respectively. The most remarkable effect is the contraction of the distance between the two topmost Fe layers below the covering Si layer. This effect is even more pronounced in the nonmagnetic HT phase.

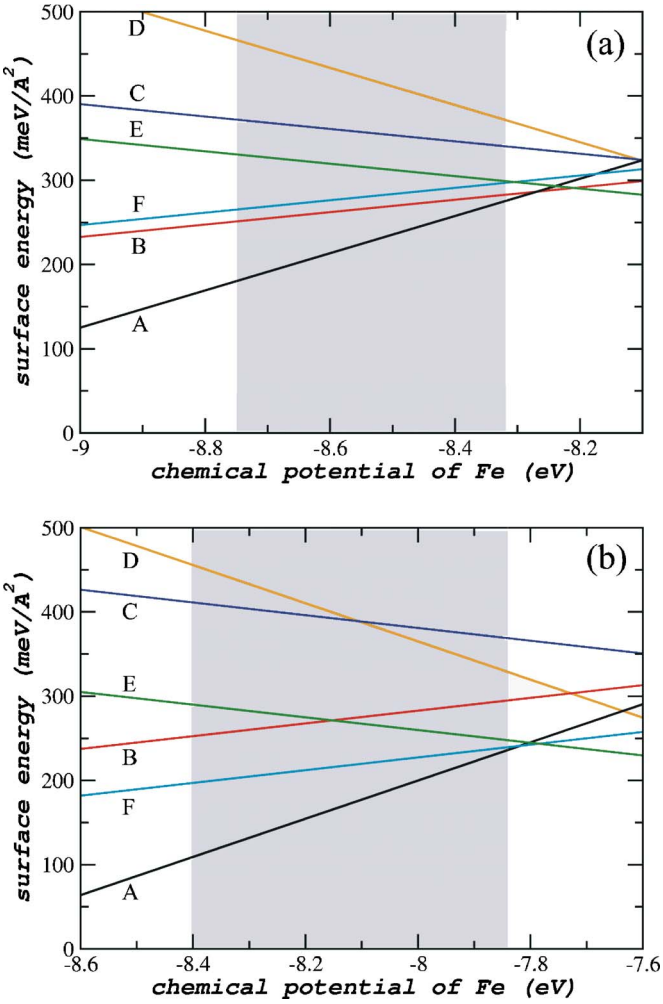

FIG. 7. (Color online) Surface free energies calculated as a function of the chemical potential for different terminations of the $Fe_3Si(111)$. (a) The top panel shows the results for ferromagnetic Fe_3Si, while (b) the bottom panel the results of a nonmagnetic calculation. The letters A–F denote different surface configurations displayed in Fig. 6.

The Si surface layer shows only a very modest relaxation (−1.8%), but the following Fe layers relax by −87% and +75%, respectively. In the relaxed final configuration, the vertical distance between these two layers is only 0.1 Å such that the two layers merge into a single layer with a honeycomb structure and with a slight corrugation of 0.1 Å. The Si surface atoms occupy the hexagonal hollows of this compact Fe layer. If Fe in the third layer is replaced to a large extent by Si antistructure atoms, this relaxation pattern is likely to be substantially modified—hence, a quantitative LEED analysis would be particularly interesting for this surface.

In the stable model (A), the magnetic moments of the first three Fe layers covered by a Si overlayer are reduced to the values $0.95\mu_B$, $2.31\mu_B$, and $1.21\mu_B$, starting from the top of the slab. Hence, the magnetic moment of the low-spin Fe atom in the subsurface position is further reduced. For comparison, on a surface terminated by an Fe trilayer [model (D)] all these magnetic moments are enhanced to $2.78\mu_B$, $2.45\mu_B$, and $2.13\mu_B$, i.e., far beyond the corresponding magnetic moments in bulk $D0_3$. Hence, the presence of a capping Si layer has a profound influence on the magnetization of the nearby Fe atoms.

VII. DISCUSSION AND CONCLUDING REMARKS

We have presented a detailed analysis of the composition, stability, and geometrical and magnetic properties of the three low-index surfaces of $D0_3$-type Fe_3Si based on *ab initio* density functional calculations combined with a statistical-mechanical analysis in the grand-canonical ensemble. Our study demonstrates that the compositional and structural phase transitions reported for these surfaces are triggered by the magnetic phase transitions of the bulk material. For both the LT and HT phases, a tendency toward Si enrichment at the surface is observed, in general agreement with experiment. Whenever a bulklike surface termination by a pure-Si layer [as on the (111) surface] or by a mixed layer containing Fe and Si in a 50:50 ratio [as on the (100) surface] is possible, this determines the stable configuration. On the (110) surface, the surface layer also has a 50:50 composition ratio, but at the expense of the formation of Si antisite defects on the γ sublattice. That Si_γ antistructure atoms are formed and not substitutional defects on the α sublattice agrees with the defect formation energies calculated for bulk Fe_3Si.

The most prominent change in the surface composition between the ferromagnetic LT phase and the nonmagnetic HT phase is predicted for the (100) surface. Whereas in the LT phase configuration (A) with a mixed layer on top of an Fe layer is stable over the entire range of chemical potentials, in the HT phase the composition of the surface layer varies with the chemical potential, from 75% Si at low values of the chemical potential of Fe [model (E)] to 100% Fe in the Fe-rich limit [model (B)]. For the (110) surface, our calculations predict the same chemical composition in the surface and subsurface layers in both phases (which agrees with the experimental result for the LT phase). The HT phase identified by the LEED studies differs from the LT phase by the formation of surface vacancies and an increased substitutional disorder in the first two subsurface layers—these changes have not been tested by our calculations on rather small surface cells. On the (111) surface, the phase transition does not involve any change in the surface periodicity; theory and experiment agree on a Si-terminated surface. The LT to HT transition is based on the formation of a high number of antistructure defects in the second subsurface layer—this possibility has not been tested by our models. It is evident, however, that at high temperatures the surface composition and structure will be influenced by entropic effects (both configurational and vibrational), which have not been taken into account in our study. One has to remember that the HT "CsCl" phase postulated for the near-surface layers[27] consists of two interpenetrating simple cubic sublattices—one formed by the α sublattice of the $D0_3$ structure and occupied by Fe only, and the other formed by the β and γ sublattices of $D0_3$ with a random occupation by Fe and Si. Qualitatively, the formation of such a phase agrees with the low defect formation energies calculated for the β and γ sublattices and the

much higher energies of antisite defects on the α sublattice,[19] but a quantitative analysis would require calculations with very large surface cells and thick slabs.

The structural relaxation of the surfaces depends both on the surface composition and on the magnetic state. On $Fe_3Si(100)$, surface (A) stable in the ferromagnetic state shows an inward relaxation of the surface layer, while the second interlayer distance is slightly expanded. Disappearance of magnetic ordering reverses the sign of both relaxation, but this structure is stabilized only under Fe-rich conditions. In the nonmagnetic state, surface (G) stable under medium values of the chemical potential shows a strong inward relaxation of the Fe top layer. These changes in the relaxation pattern can be attributed to the fact that the large exchange splitting of the local Fe density of states in the ferromagnetic phase also affects the Fe d-Si p hybridization and the strength of the covalent Fe-Si bonds. On the close-packed (110) surface, the stable Si-enriched surface [model (D)] undergoes only minimal relaxations, both in the LT and HT phases. In contrast, the geometric structure of the open (111) surface is strongly modified by relaxation. The general pattern is the same in both the ferromagnetic and the nonmagnetic phases: the first subsurface layer (Fe) relaxes inward [by −87% in the nonmagnetic (NM) phase and −34% in the ferromagnetic (FM) phase], while the second subsurface layer relaxes outward (by +75% and +33%, respectively). As a result, these two layers nearly collapse to form a buckled honeycomb structure. This combined layer is almost flat (buckling of 0.1 Å) in the NM state, but substantially buckled (amplitude of 0.53 Å) in the FM state. The dense Fe layer drifts away from the substrate (the interlayer spacing increases from an ideal value of 0.8–1.4 Å in the NM phase and to 1.07 Å in the FM phase), the Si atoms in the surface layer are located in the hexagonal hollows of the honeycomb, at a distance from the outmost Fe atoms close to the ideal interlayer distance.

Surface-induced changes in the magnetic moments are rather modest—generally one notes an enhancement by a few tenths of $1\mu_B$ in the surface and subsurface layers. A notable exception is again the (111) surface. Here, the magnetic moments occupying the subsurface layer are in a low-spin state, and their magnetic moment is further reduced to $0.95\mu_B$. Hence, the buckled honeycomb layer contains both high-spin ($2.31\mu_B$) and low-spin ($0.95\mu_B$) Fe atoms; this surface shows a pronounced magnetostructural effect.

Very recently, Kmiec *et al.*[46] investigated diffusion in Fe_3Si films using nuclear resonant scattering of synchrotron radiation in a grazing-incidence geometry. They report a pronounced enhancement of the diffusion constant in the near-surface region. Unfortunately, no information on the surface orientation of the film was given; hence, a detailed confrontation of this result with ours is not possible. However, the Si enrichment of the surface layers and the presence of Si antisite defects reported here certainly suggest a profound modification of the diffusion mechanism in the near-surface region.

In summary, we have presented a detailed *ab initio* study of the composition, structure, and stability of the low-index surfaces of Fe_3Si. For the ferromagnetic low-temperature phase, we predict a general tendency toward a Si enrichment of the surface, in agreement with experiment. We show that the reported surface phase transitions are strongly coupled to the magnetic phase transition in the bulk. At high temperatures, the surface structure is characterized, in addition to the magnetic effects, by an entropy-driven tendency to a disordered occupation of the β and γ sites of the $D0_3$ lattice—this agrees with the calculated defect formation energies, but a quantitative study of disorder effects has not been performed. Quite strong structural relaxation effects are predicted for the more open (100) and (111) surfaces—it would be interesting to confront these predictions with a detailed LEED analysis.

ACKNOWLEDGMENT

This work has been supported by Project "Software Lizenzen VASP" FA 513 901.

*Email address: juergen.hafner@univie.ac.at
†Email address: daniel.spisak@univie.ac.at

[1] S. P. Murarka and M. C. Peckerar, in *Electronic Materials, Science and Technology*, edited by J. Streichen (Academic, Boston 1989), p. 267.
[2] J. E. Mattson, S. Kumar, E. E. Fullerton, S. R. Lee, C. H. Sowers, M. Grimsditch, S. D. Bader, and F. T. Parker, Phys. Rev. Lett. **71**, 185 (1993).
[3] K. Inomata, K. Yusu, and Y. Saito, Phys. Rev. Lett. **74**, 1863 (1995).
[4] J. Herfort, H. P. Schönherr, A. Kawaharzuka, M. Ramsteiner, and K. H. Ploog, J. Cryst. Growth **278**, 666 (2005).
[5] K. Lenz, E. Kosubek, K. Baberschke, H. Wende, J. Herfort, H. P. Schönherr, and K. H. Ploog, Phys. Rev. B **72**, 144411 (2005).
[6] K. J. Friedland, M. Bowen, J. Herfort, H. P. Schönherr, and K. H. Ploog, J. Phys.: Condens. Matter **18**, 2641 (2006).
[7] A. Ionescu, C. A. F. Vaz, T. Tripiniotis, C. M. Gurtler, H. Garcia-Miquel, J. A. C. Bland, M. E. Vickers, R. M. Dalgliesh, S. Langridge, Y. Bugoslavsky, Y. Miyoshi, L. Cohen, and K. R. A. Ziebeck, Phys. Rev. B **71**, 094401 (2005).
[8] O. Schneeweis, N. Pizúrová, Y. Jirásková, T. Žál, and B. Cornut, J. Magn. Magn. Mater. **251-216**, 115 (2000).
[9] M. Hansen, *Constituion of Binary Alloys* (McGraw-Hill, New York, 1958).
[10] T. B. Massalski, *Binary Alloy Phase Diagrams* (American Society for Metals, Metals Park, OH, 1986).
[11] O. Kubaschewski, *Iron Binary Phase Diagrams* (Springer, Berlin, 1982).
[12] P. Villars and L. D. Calvert, *Pearson's Handbook of Crystallographic Data for Intermetallic Phases*, 2nd ed. (ASM International, Materials Park, OH, 1991).
[13] E. G. Moroni, W. Wolf, J. Hafner, and R. Podloucky, Phys. Rev. B **59**, 12860 (1999).
[14] B. Sepiol and G. Vogl, Phys. Rev. Lett. **71**, 731 (1993).

[15] G. Vogl and B. Sepiol, Acta Metall. Mater. **42**, 3175 (1994).
[16] A. Gude and H. Mehrer, Philos. Mag. A **76**, 1 (1997).
[17] H. Mehrer, M. Eggersmann, A. Gude, M. Salamon, and B. Sepiol, Mater. Sci. Eng., A **240**, 889 (1997).
[18] B. Sepiol, A. Meyer, G. Vogl, H. Franz, and R. Ruffer, Phys. Rev. B **57**, 10433 (1998).
[19] S. Dennler and J. Hafner, Phys. Rev. B **73**, 174303 (2006).
[20] H. von Känel, K. A. Mäder, E. Müller, N. Onda, and H. Sirringhaus, Phys. Rev. B **45**, 13807 (1992).
[21] J. J. Hinarejos, G. R. Castro, P. Segovia, J. Alvarez, E. G. Michel, R. Miranda, A. Rodgriguez-Marco, D. Sanchez-Portal, E. Artacho, F. Yndurain, S. H. Yang, P. Ordejon, and J. B. Adams, Phys. Rev. B **55**, R16065 (1997).
[22] H. Sirringhaus, N. Onda, E. Müller-Gubler, P. Müller, R. Stalder, and H. von Känel, Phys. Rev. B **47**, 10567 (1993).
[23] U. Starke, W. Weiss, M. Kutschera, R. Bandorf, and K. Heinz, J. Appl. Phys. **91**, 6154 (2002).
[24] N. Onda, H. Sirringhaus, S. Goncalves-Conto, C. Schwartz, S. Zehnder, and H. von Känel, Appl. Surf. Sci. **73**, 124 (1993).
[25] H. Busse, J. Kandler, B. Eltester, K. Wandelt, G. R. Castro, J. J. Hinarejos, P. Segovia, J. Chrost, E. G. Michel, and R. Miranda, Surf. Sci. **381**, 133 (1997).
[26] U. Starke, W. Meier, C. Rath, J. Schardt, W. Weiss, and K. Heinz, Surf. Sci. **377-379**, 539 (1997).
[27] U. Starke, J. Schardt, W. Weiss, W. Meier, C. Polop, P. L. de Andres, and K. Heinz, Europhys. Lett. **56**, 822 (2001).
[28] S. Walter, R. Bandorf, W. Weiss, K. Heinz, U. Starke, M. Strass, M. Bockstedte, and O. Pankratov, Phys. Rev. B **67**, 085413 (2003).
[29] M. Vondráček, V. Dudr, N. Tsud, P. Lejček, V. Cháb, K. C. Prince, V. Matolín, and O. Schneeweis, Surf. Sci. **600**, 4108 (2006).
[30] G. Kresse and J. Furthmüller, Phys. Rev. B **54**, 11169 (1996); Comput. Mater. Sci. **6**, 15 (1996).
[31] P. E. Blöchl, Phys. Rev. B **50**, 17953 (1994).
[32] J. P. Perdew and A. Zunger, Phys. Rev. B **23**, 5048 (1981).
[33] J. P. Perdew, K. Burke, and K. Ernzerhof, Phys. Rev. Lett. **77**, 3865 (1996).
[34] H. J. Monkhorst and J. D. Pack, Phys. Rev. B **13**, 5188 (1976).
[35] M. Methfessel and A. T. Paxton, Phys. Rev. B **40**, 3616 (1989).
[36] P. Becker, Metrologia **40**, 366 (2003).
[37] M. Acet, H. Zähres, E. F. Wassermann, and W. Pepperhoff, Phys. Rev. B **49**, 6012 (1994).
[38] S. N. Vaboya and G. C. Kennedy, J. Phys. Chem. Solids **31**, 2329 (1970).
[39] C. Kittel, *Introduction to Solid State Physics*, 6th ed. (Wiley, New York, 1986).
[40] V. A. Niculescu, T. J. Burch, and J. I. Budnick, J. Magn. Magn. Mater. **39**, 223 (1983).
[41] J. A. Rayne and B. S. Chandrasekhar, Phys. Rev. **122**, 1714 (1961).
[42] H. G. Drickamer, R. W. Lynch, R. L. Clendenen, and E. A. Perez-Albuerne, Solid State Phys. **19**, 1359 (1966).
[43] G. X. Qian, R. M. Martin, and D. J. Chadi, Phys. Rev. B **38**, 7649 (1988).
[44] M. W. Finnis, Phys. Status Solidi A **166**, 397 (1998).
[45] K. Reuter and M. Scheffler, Phys. Rev. B **65**, 035406 (2002).
[46] D. Kmiec, B. Sepiol, M. Sladecek, G. Vogl, J. Korecki, T. Slezak, R. Rüffer, K. Vanormelingen, and A. Vantomme, Defect Diffus. Forum **237-240**, 1222 (2005).